Available online at www.sciencedirect.com
ScienceDirect
Trans. Nonferrous Met. Soc. China 35(2025) 169−183
Transactions of Nonferrous Metals Society of China
www.tnmsc.cn

Predictor−corrector inverse design scheme for property−composition prediction of amorphous alloys

Tao LONG[1], Zhi-lin LONG[2], Bo PANG[1]

1. School of Mechanical Engineering and Mechanics, Xiangtan University, Xiangtan 411105, China;
2. School of Civil Engineering, Xiangtan University, Xiangtan 411105, China

Received 22 May 2023; accepted 23 February 2024

Abstract: In order to develop a generic framework capable of designing novel amorphous alloys with selected target properties, a predictor−corrector inverse design scheme (PCIDS) consisting of a predictor module and a corrector module was presented. A high-precision forward prediction model based on deep neural networks was developed to implement these two parts. Of utmost importance, domain knowledge-guided inverse design networks (DKIDNs) and regular inverse design networks (RIDNs) were also developed. The forward prediction model possesses a coefficient of determination (R^2) of 0.990 for the shear modulus and 0.986 for the bulk modulus on the testing set. Furthermore, the DKIDNs model exhibits superior performance compared to the RIDNs model. It is finally demonstrated that PCIDS can efficiently predict amorphous alloy compositions with the required target properties.
Key words: amorphous alloys; machine learning; deep neural networks; inverse design; elastic modulus

1 Introduction

In 1960, KLEMENT et al [1] first discovered an Au−Si amorphous alloy. Amorphous alloys, also known as metallic glasses, have good mechanical, electrical, soft magnetic, and electrochemical properties compared to conventional alloys [2−4]. After decades of development, amorphous alloys have been widely used in aerospace, transformers and military fields [5−7]. Nevertheless, the lack of a theoretical basis for the correlation between composition and properties has greatly hindered the development of amorphous alloys. In the conventional design of amorphous alloys, the approach to achieving the target property index conventionally involves continuously adjusting the composition ratio of elements through extensive experimental verification [8−10]. This traditional "trial-and-error" approach is flawed because it requires a considerable time, manpower and material resources and does not always guarantee success.

In recent years, with the development of computer technology, machine learning (ML) has been widely used in the field of alloys [11]. For instance, YANG et al [12] proposed a ML-based alloy design system (MADS) to facilitate the rational design of high-entropy alloys (HEAs). WU et al [13] established the density-fluctuation model of local structural instability in amorphous alloys via ML. And SAMAVATIAN et al [14] discovered novel quaternary bulk metallic glasses (BMGs) by using the ML technique. Furthermore, several studies have used the ML method to predict the glass-forming ability (GFA) of amorphous alloys and the predictions are in good agreement with experimental values [15−20].

The above studies have developed forward prediction models from material composition or

Corresponding author: Zhi-lin LONG, Tel: +86-731-58298287, E-mail: longzl@xtu.edu.cn
https://doi.org/10.1016/S1003-6326(24)66672-0

structure to target properties. However, forward prediction models are only applicable to problems with small composition spaces, and once the composition space is very large, it is not feasible to explore all possible combinations of composition with forward ML prediction models. The main reason is the lack of efficient methods for proactively designing promising candidate compositions, rather than exploring the entire composition space [21]. Therefore, an idea naturally arises: is a prediction path from material target properties to material composition properties feasible? This can be defined as an inverse design problem, where the target properties of the material are used as inputs for the inverse calculation of the material composition [22]. The inverse design approach avoids searching the entire composition space for candidate materials and enables the inverse design of material compositions based on user-specified material target properties. For example, POLLOK et al [23] used six different standard convolutional neural network (CNN) models to inversely predict the target properties (magnetization, size and location) of a single hard magnet in a specific 2-D magnetic field. JIANG et al [24] used conditional generative adversarial network (cGAN) to establish an inverse design scheme for the dispersion relation and near-optimal structure of elastic metamaterials. WANG et al [25] proposed machine learning design system (MLDS) for the performance-oriented compositional design of high-performance complex copper alloys. In summary, ML-based inverse design approaches or techniques present attractive prospects in rational material design.

Currently, there are few studies on designing amorphous alloys using inverse design techniques. ZHOU et al [26] implemented inverse design based on a dataset of four systems of BMGs using a generative model of generative adversarial network (GAN). However, the above study used only four systems of BMGs and the new data generated were limited to this system. Moreover, for small datasets or when it is not possible to use data from the whole domain, the use of standard GAN models lacks robustness and has difficulty in reaching Nash equilibrium, and its generation results make it difficult to resist the effect of noise [27]. For this reason, in addition to the use of GAN models, it is crucial to develop new generative models for small data sets, which can be done by constructing appropriate loss functions [28]. Additionally, integrating domain knowledge into ML can significantly reduce data requirements and improve the reliability and robustness of ML [29,30]. For instance, WEI et al [31] found highly explanatory formulas describing the high-temperature oxidation behavior of FeCrAlCoNi-based HEAs based on domain knowledge-guided ML. LI et al [32] proposed a domain knowledge-based ML method to predict the saturated magnetization and critical diameter of soft magnetic amorphous alloys, and the results showed that the ML model outperformed the conventional prediction methods.

This work presents a new method of predictor−corrector inverse design scheme (PCIDS), which consists of a predictor module and a corrector module, for guiding the inverse design of amorphous alloys. Figure 1 shows the framework diagram of this work. To demonstrate the universality of our constructed inverse design scheme, we conducted case tests on a BMGs dataset containing 28 different systems with 49 different elements (see Fig. 1(a)). The elastic moduli as the target property were successfully implemented by the developed inverse design algorithm. Especially, PCIDS is not only applicable to the elastic moduli as a target property but also to other properties, such as the critical casting diameter (D_{max}) as an assessment of the GFA of amorphous alloys. Moreover, the PCIDS is also applicable to other material fields. It is conceivable that this research work will greatly accelerate the development of amorphous alloys.

2 Methods

2.1 Data collection

The elastic modulus is a basic physical quantity that characterizes elasticity, which includes Young's modulus (E), Poisson's ratio (ν), shear modulus (G) and bulk modulus (K). There is a correlation among these four elastic moduli, where E and ν can be expressed by K and G through the following equations [33,34]:

$$E = \frac{9KG}{3K+G} \tag{1}$$

$$\nu = \frac{1}{2}(3K-2G)/(3K+G) \tag{2}$$

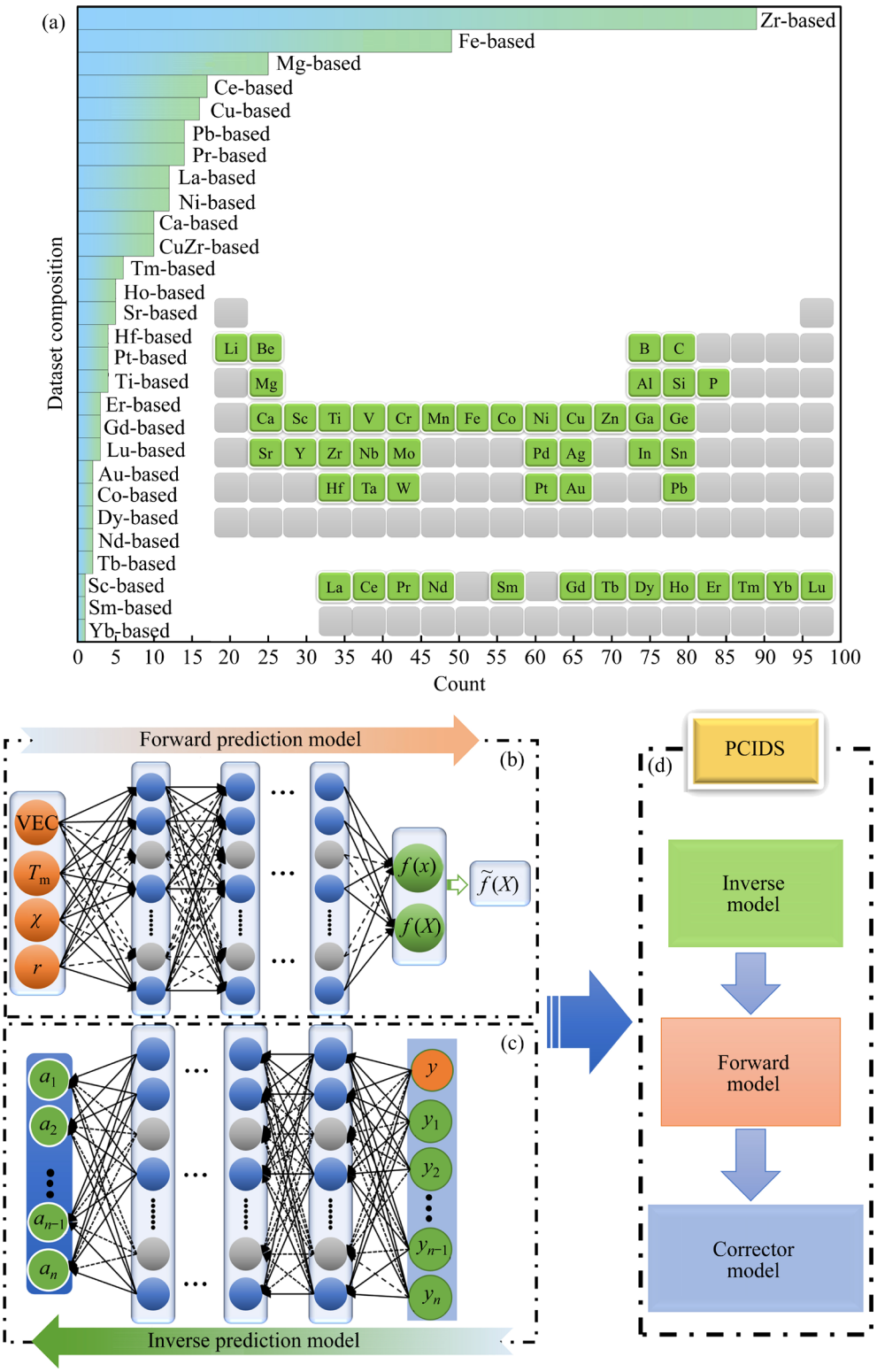

Fig. 1 Overall workflow for efficient design of amorphous alloys: (a) Collection and analysis of dataset; (b) Forward prediction model; (c) Inverse prediction model; (d) Workflow of PCIDS

The ratio of G to K is closely related to the fracture toughness, intrinsic plasticity, and GFA of amorphous alloys [33]. And it can be known from the literature [35,36] that there is a strong linear relationship between yield shear stress and G, fracture tensile strength, hardness and E. This work therefore takes the target properties of G and K as an example to realize the inverse design of amorphous alloys. The 318 amorphous alloys containing K and G are collected from the reported

literature [33,37−39] and the dataset is listed in Table S1 of Supplementary Information. As shown in Fig. 1(a), the entire dataset contains 28 different amorphous alloy systems, with the largest proportion of Zr-based alloys. The subplots in Fig. 1(a) exhibit the distribution of K and G and the distribution of the contained elements.

2.2 Architecture design of forward prediction model

Primarily, we establish the forward predictive mapping f from the structure to the elastic modulus via deep neural networks (DNNs). For a given set of structural data X of amorphous alloys, the K or G can be predicted by the mapping f:

$$f(X)=K \text{ (or } G) \tag{3}$$

Two key technical points are involved here: the selection of structural descriptors for amorphous alloys and the design of the DNN model structure. For the first point, from reference [37,38,40], we chose four structural descriptors as the input features X of the model, as given in Table 1. For the second point, Fig. 1(b) shows the structure of the forward model for predicting K or G. As with the usual configuration of fully connected neural networks, the model contains an input layer, hidden layers, and an output layer. However, for the output layer, we make a new design, i.e., the two results are output and then the average is taken to obtain the final prediction result $\tilde{f}(X)$. Since DNN models are prone to overfitting risk, the Dropout method is used to prevent overfitting [41]. The core of the method is to discard neurons randomly in the hidden layer with probability p (as shown in Fig. 1(b), the discarded neurons are indicated by the gray circles).

Table 1 Four structural descriptors of amorphous alloys

Description	Equation
Averaged valance electron	$\mathrm{VEC}=\sum_{i=1}^{n} a_i \mathrm{VEC}_i$
Averaged melting point	$T_\mathrm{m}=\sum_{i=1}^{n} a_i T_{\mathrm{m}(i)}$
Averaged electronegativity	$\chi=\sum_{i=1}^{n} a_i \chi_i$
Averaged atomic radius	$r=\sum_{i=1}^{n} a_i r_i$

a_i, VEC_i, $T_{\mathrm{m}(i)}$, χ_i and r_i are the atomic fraction, valance electron, melting point, electronegativity and atomic radius for each constituent element, respectively.

2.3 Architecture design of inverse prediction model

The purpose of the inverse design problem is to obtain a mapping f^{-1} based on the desired target properties of an amorphous alloy composed of several elements and to be able to predict the atomic fraction of these elements by

$$f^{-1}(\boldsymbol{Y})=A \tag{4}$$

where $\boldsymbol{Y}=(y, y_1, y_2, \cdots, y_n)$ represents a vector consisting of element types $y_1, y_2, \cdots, y_n$ and the target properties y. In order to make the elements available for calculation, y_i (i=1, 2, ⋯, n) denotes the relative atomic mass of the i-th element. $\boldsymbol{A}=(a_1, a_2, \cdots, a_n)$ represents the predicted atomic fraction of each element.

In general, it is common to use the mean square error (MSE) as the loss function in regression problems [21,42]. Recently, deep learning based on physical information and theoretical guidance has been widely used in solving differential equations [43,44]. Apart from using MSE, physical constraints such as initial marginal value conditions or prior knowledge of the relevant differential equations are embedded in the loss functions to improve the performance of deep learning models. Thus, in this work, we provide a new loss function for the inverse design of amorphous alloys based on a combination of domain knowledge and MSE. It is known from domain knowledge that the sum of the atomic fractions of all elements in a given alloy composition is equal to 100%. Thus, the new loss function is given as follows:

$$\mathrm{Loss}_\mathrm{new}=\mathrm{Loss}_1+\alpha\mathrm{Loss}_2 \tag{5}$$

$$\mathrm{Loss}_1=\frac{1}{N}\sum_{i=1}^{N}\|\tilde{\boldsymbol{A}}_i-\boldsymbol{A}_i\|_2^2 \tag{6}$$

$$\mathrm{Loss}_2=\frac{1}{N}\sum_{i=1}^{N}\left|\|\boldsymbol{A}_i\|_1-100\right|^2 \tag{7}$$

where $\alpha\in(0,1)$ is the weight value assigned, N represents the number of training samples, $\|\cdot\|_2$ and $\|\cdot\|_1$ denote the L2 and L1 norm of the vector, respectively. $\tilde{\boldsymbol{A}}_i$ and $\boldsymbol{A}_i$ are the experimental atomic fractions and the predicted atomic fractions of alloy composition, respectively. Figure 1(c) shows the overall framework flow of the inverse design. The use of $\mathrm{Loss}_\mathrm{new}$ and MSE as loss functions are denoted as domain knowledge-guided inverse

design networks (DKIDNs) and regular inverse design networks (RIDNs), respectively.

2.4 Model evaluation indexes

The evaluation metrics used to evaluate the prediction performance of the model are the coefficient of determination (R^2) and root mean square error (RMSE) as follows:

$$R^2 = 1 - \frac{\sum_{i=1}^{n}\left(y_i - f_i(X)\right)^2}{\sum_{i=1}^{n}\left(y_i - \overline{y}\right)^2} \tag{8}$$

$$\mathrm{RMSE} = \sqrt{\sum_{i=1}^{n}\frac{1}{n}\left(f_i(X) - y_i\right)^2} \tag{9}$$

where y_i, $f_i(X)$ and $\overline{y}$ are the measured, predicted and average values of K or G, respectively. Since the four input features have different ranges and scales, it is necessary to speed up the training and convergence of the model. The input features are preprocessed by the following equation:

$$x' = \frac{x - \mu}{\sigma} \tag{10}$$

where x' is the value after processing, μ and σ are the mean and standard deviation of x, respectively.

For the inverse design evaluation index, we use the following formulations:

$$\overline{R}^2 = \frac{1}{N}\sum_{i=1}^{N} R_i^2 \tag{11}$$

$$\overline{\mathrm{RMSE}} = \sqrt{\frac{1}{N}\sum_{i=1}^{N} |\,\tilde{\boldsymbol{A}}_i - \boldsymbol{A}_i\,|_2^2} \tag{12}$$

where R_i^2 denotes coefficient of determination of the atomic fraction of the i-th sample.

3 Results and discussion

3.1 Forward prediction results of elastic properties

The 318 data samples collected are randomly divided into 80% as the training set and 20% as the test set. In DNNs, hyperparameters such as the number of neurons, the number of hidden layers, and the dropout rate (p) have a significant impact on the model performance. To obtain the optimal model, a five-fold cross-validation (CV) based on the training set is used to evaluate the model's performance under different combinations of hyper-parameters. Figure 2 shows the entire prediction workflow. Throughout the model training phase, Adam is used as the optimizer and the ReLU function is employed as activation function [45]. Through several experiments, the effects of the values of various hyperparameters on the model performance are displayed in Fig. S1 of Supplementary Information. The optimal hyper-parameter combinations are listed in Table 2. The detailed structure of the optimal forward prediction model is shown in Fig. S2 of Supplementary Information. As shown in Fig. 3(a), the optimal forward prediction model for predicting K exhibits good generalization performance on the test set, with regression metrics R^2 and RMSE of 0.986 and 6.630, respectively. The colour scale shows that only three samples have large errors. Furthermore, the subplot illustrates the model's performance on the training set, with R^2 and RMSE values of 0.987 and 6.219, respectively. Notably, only two samples exhibit substantial training errors. In addition, as depicted in Fig. 3(b), the optimal forward prediction model demonstrates even better generalization ability for predicting G on the test set, achieving impressive regression metrics with R^2 and RMSE values of 0.990 and 2.164, respectively. It is interesting to note that only one sample exhibits significant errors. Moreover, the model also exhibits remarkable performance in the training set, with R^2 and RMSE values of 0.992 and 1.806, respectively. In conclusion, with just four descriptors as input, the optimal forward prediction model can achieve high-precision predictions for both K and G.

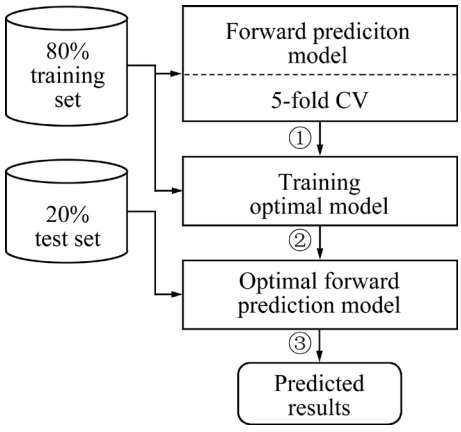

Fig. 2 Flow chart of forward prediction model for K and G

Table 2 Hyperparameter combinations in optimal forward prediction models

Model	Optimal hyperparameter combination
$f(X)=G$	Number of hidden layers: 2, number of neurons in hidden layer: 450, p=1.0, learning rate: 0.007, and epoch: 2000
$f(X)=K$	Number of hidden layers: 2, Number of neurons in hidden layer: 600, p=0.1, learning rate: 0.009, and epoch: 2100

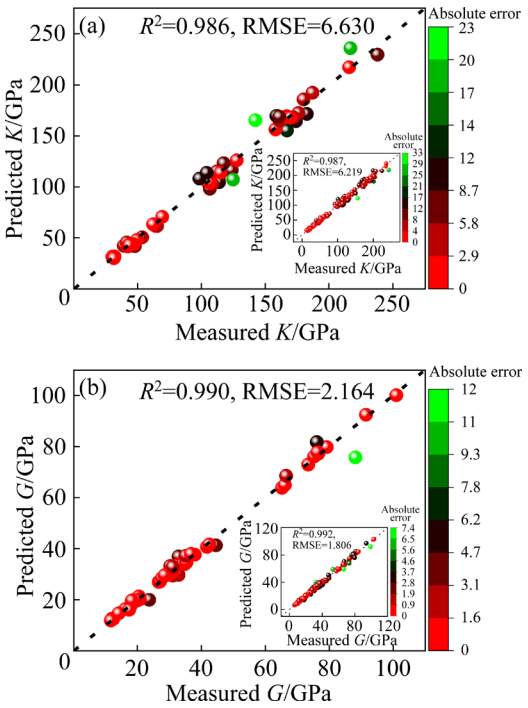

Fig. 3 Comparison between measured and predicted values by optimal forward prediction model for K (a) and G (b) (Subplots represent the results of the training set)

We compare the elastic forward prediction model based on DNNs in this work with other current ML models, as shown in Table 3. It can be found that the model developed in this work only needs four input descriptors to achieve the highest prediction accuracy. The forward prediction model has a better ability to extract feature information than the shallow ML model and analyzes the complex mapping relationship between input features and output results through the hidden layer.

Next, to elucidate how the four features affect K and G, the SHapley Additive exPlanations (SHAP) method was introduced to explain the model, a new unified approach proposed by LUNDBERG and LEE in 2017 [47] for explaining ML prediction models with “black box” properties. The more influence a feature has on the prediction result, the more significance it holds. The average of the absolute SHAP values of a feature can be considered as the importance of that feature. The importance ranking of the four features affecting the prediction of K and G is shown in Fig. 4. The interesting finding is that the average atomic radius r plays the most important role in predicting both K and G. It can be seen that for prediction of K, the importance of features r, T_m, VEC and χ decreases sequentially. Additionally, for prediction of G, the importance of features r, VEC, χ and T_m decreases in order.

Table 3 R^2 values of developed models in this work and previously reported ML models

No.	Model	Number of features	Refs.	G	K
1	SVR	5	[46]	0.961	0.975
2	RF	4	[37]	0.967	0.968
3	SR	4	[37]	0.908	0.956
4	Lasso	35	[38]	0.986	0.984
5	XGBoost	9	[38]	0.983	0.971
6	DNNs	4	This work	0.990	0.986

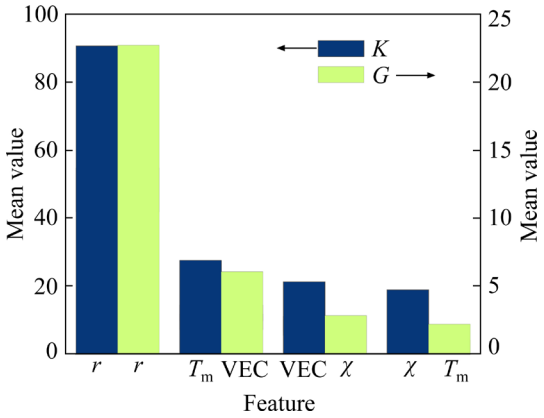

Fig. 4 Feature importance ranked by SHAP method for K and G

It is well known that atomic radius is negatively correlated with atomic bonds. And in amorphous alloy systems, the modulus is closely related to the constituent elements and their atomic bonds [48,49]. As is evident from Fig. 4, the interesting finding is that the average atomic radius r is the most important factor among these four features for predicting K and G. To further understand how r affects K and G, Fig. 5 demonstrates the relationship between r values and their SHAP values. It is very obvious that the

feature r shows a negative correlation with its SHAP value. In other words, it means that K and G are negatively correlated with the average atomic radius r. This result can also be directly or indirectly corroborated by a number of studies [50,51]. It is important to note that SHAP values greater than 0 positively affect K and G, while SHAP values less than 0 negatively affect them. In other words, r exerts a positive influence on K and G when r<147 pm, while r exerts a negative influence on K and G when r>147 pm.

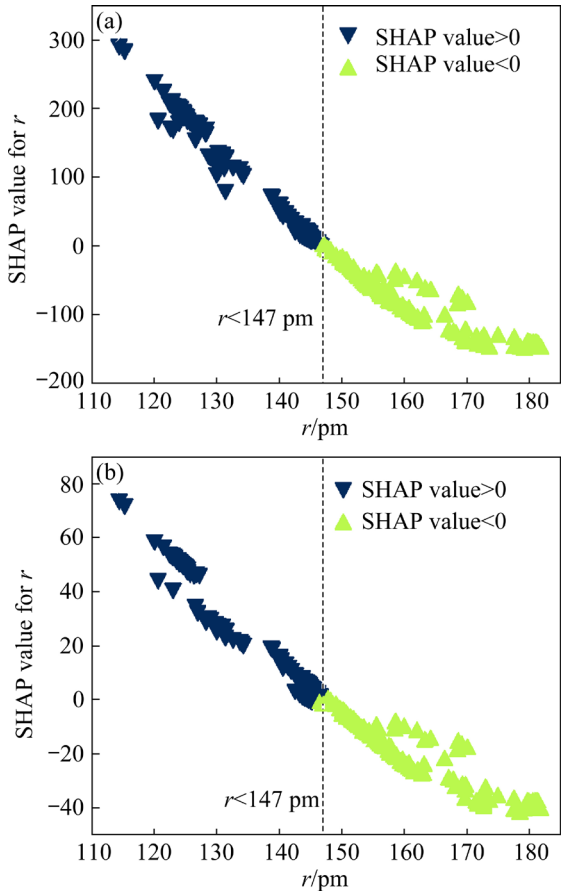

Fig. 5 SHAP value changes with r for K (a) and G (b)

3.2 Inverse design scheme

As a case demonstration, we use constructed inverse design framework to implement the inverse mapping of the target properties (K and G) to the corresponding atomic fractions of the elements and to evaluate quantitatively the model.

3.2.1 Modelling process for inverse design

Firstly, the collected 318 data samples are randomly divided into 80% training set and 20% test set. Figure 6 shows the distribution of 318 amorphous alloys containing 2, 3, 4, 5, 6 and 7 elements. It is observed that the amorphous alloys in the dataset contain at most 7 elements, so n=7. That is to say, for mapping f^{-1}, the input feature is $\boldsymbol{Y}$=(G, K, y_1, y_2, ⋯, y_7) and the output result is $\boldsymbol{A}$=(a_1, a_2, ⋯, a_7). For convenience of model building and training, when the element content in the amorphous alloys is below 7, its remaining input features are replaced with 0. For example, the input feature is $\boldsymbol{Y}$=(26.8, 102.2, 91.224, 26.982, 58.643, 63.564, 0, 0, 0) for alloy $Zr_{68}Al_8Ni_8Cu_{16}$. Therefore, depending on this characteristic of the input features, we can actively constrain the output results during the training process of the model. For input features containing 0, the corresponding positions of the corresponding output results can be adjusted to be 0. For example, for alloy $Zr_{68}Al_8Ni_8Cu_{16}$, if the output result is $\boldsymbol{A}$=(a_1, a_2, a_3, a_4, a_5, a_6, a_7), then the result can be adjusted to be $\boldsymbol{A}$=(a_1, a_2, a_3, a_4,0, 0, 0). Figure 7 visualizes the detailed flow of the specific implementation of the DKIDNs (or RIDNs) model, and Algorithm 1 represents the process of the proposed DKIDNs (or RIDNs) algorithm in pseudo-code.

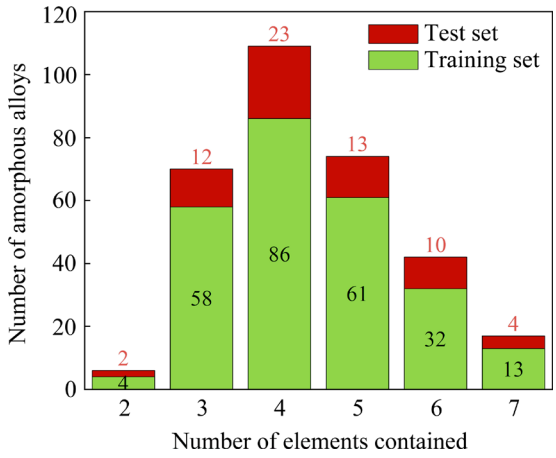

Fig. 6 Number of amorphous alloys containing 2, 3, 4, 5, 6 and 7 elements

Algorithm 1: DKIDNs (or RIDNs) model with constraints

Input: Input features $\boldsymbol{Y}$=(G, K, y_1, y_2, ⋯, y_7) and the related hyperparameters;

Output: Predicted results $\boldsymbol{A}$=(a_1, a_2, ⋯, a_7);

1. The dataset is divided into 80% training set and 20% test set;

2. M_{train} ← Training set features Y_{train}, M_{test} ← Test set features Y_{test};

3. B_{train} ← Counting the number of zero elements in M_{train};

4. B_{test} ← Counting the number of zero elements in M_{test};

5. H_{train} ← Counting the number of samples in M_{train};
6. H_{test} ← Counting the number of samples in M_{test};
7. Standardize Y_{train}, and Y_{test} using the Eq. (10);
8. for *epoch* ← *0* **to** *max epoch* **do**
9. $A_{Predicted}$ ← *Prediction results are obtained based on the current sample*;
10. for i ← *0* **to** H_{train} **do**
11. $A_{Predicted}[i,7-B_{train}[i]:]$ ← 0;
12. end
13. Calculate the error based on the Eq. (5) (or MSE);
14. Update the weights and biases in the DNNs;
15. end
16. Save the trained model;
17. Loading Models;
18. for i ← *0* **to** H_{test} **do**
19. $A_{Predicted}[i,7-B_{test}[i]:]$ ← 0;
20. end
21. return result

3.2.2 Hyperparameter selection of model

In order to obtain the optimal model, we divide 10% of the data from the training set as the validation set to adjust the hyperparameters. To observe the prediction performance of the DKIDNs and RIDNs models for the validation set with different hyperparameters, the dropout rate p is set to be 0.2 and the learning rate to be 0.01. Figure 8 shows the prediction performance of the DKIDNs and RIDNs models in the validation set. From Fig. 8(a), it can be found that for models DKIDNs and RIDNs, the best prediction performance is obtained when the number of hidden layers is 3 and 4, respectively. However, as the number of hidden layers increases, the $\overline{R}^2$ score decreases substantially, which indicates that both models are in an overfitting state. From Fig. 8(b), it can be observed that for the DKIDNs model, the best $\overline{R}^2$ score is 0.932 when the hidden layer contains 210 neurons, and for the RIDNs model the best $\overline{R}^2$ score is 0.920 when the hidden layer contains 310 neurons. Figure 9 shows the prediction accuracy of DKIDNs model for different values of α. The DKIDNs model has the best prediction performance when α is 0.2. In summary, the hyperparameter values of the best model are summarized in Table 4. And the detailed structure of the optimal DKIDNs and RIDNs models is shown in Fig. S3 of Supplementary Information.

3.2.3 Prediction results of DKIDNs and RIDNs models

After finding the optimal hyperparameters, we aim to evaluate the generalization ability of the proposed inverse design model in the test set. Firstly, we evaluate the prediction performance of the model from a global viewpoint. Since the test set contains 64 alloys, each alloy contains up to 7 elements, i.e., the predicted values can be summarized as a 64×7 matrix. In order to visualize

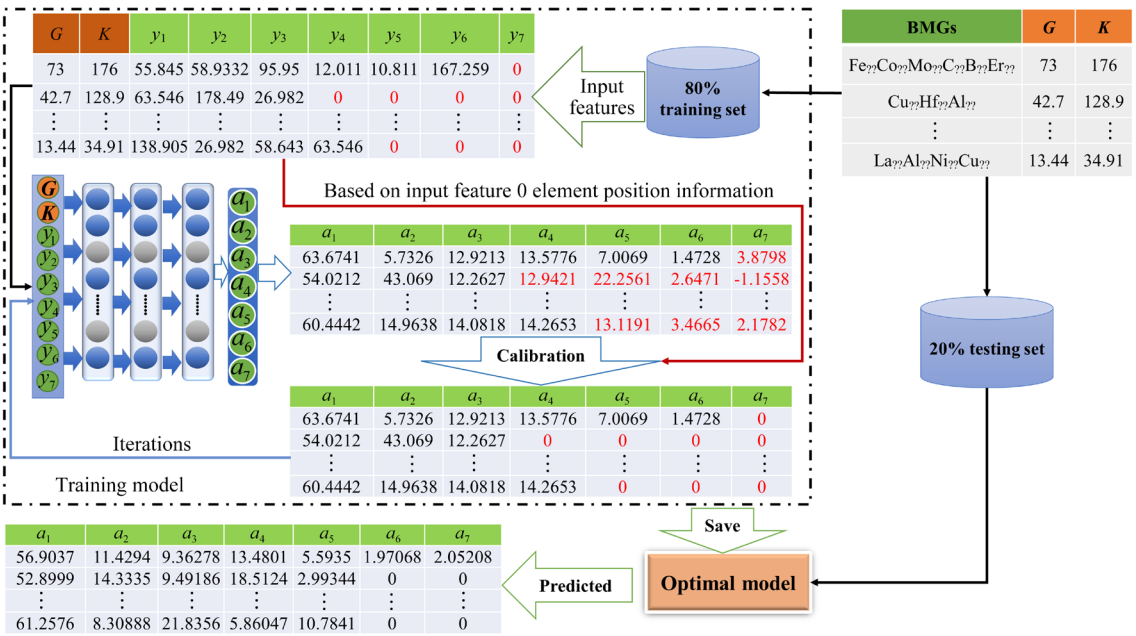

Fig. 7 Detailed flow of specific implementation of DKIDNs (or RIDNs) model

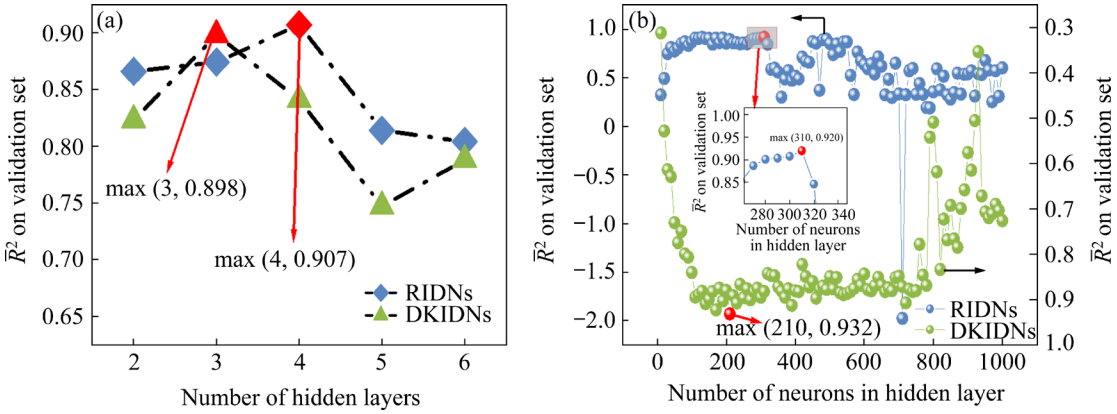

Fig. 8 Prediction results on validation set by DKIDNs and RIDNs models with different numbers of hidden layers (a) and different numbers of neurons in hidden layer (b)

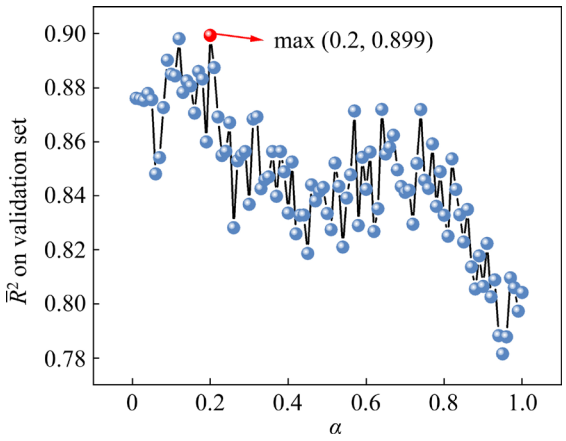

Fig. 9 Prediction results on validation set by DKIDNs model with different values of α

Table 4 Hyperparameter combinations in optimal prediction models

Model	Optimal hyperparameter combination
DKIDNs	Number of hidden layers: 3, number of neurons in hidden layer: 210, p=0.2, learning rate: 0.01, α=0.2, and epoch: 2800
RIDNs	Number of hidden layers: 4, number of neurons in hidden layer: 310, p=0.2, learning rate: 0.01, and epoch: 2800

the prediction results so as to intuitively observe the prediction performance of the DKIDNs and RIDNs models, we plot the prediction results into a two-dimensional cloud plot, as shown in Fig. 10. Intuitively, the two-dimensional cloud plots drawn from the data predicted by the DKIDNs and RIDNs models are roughly similar to the two-dimensional

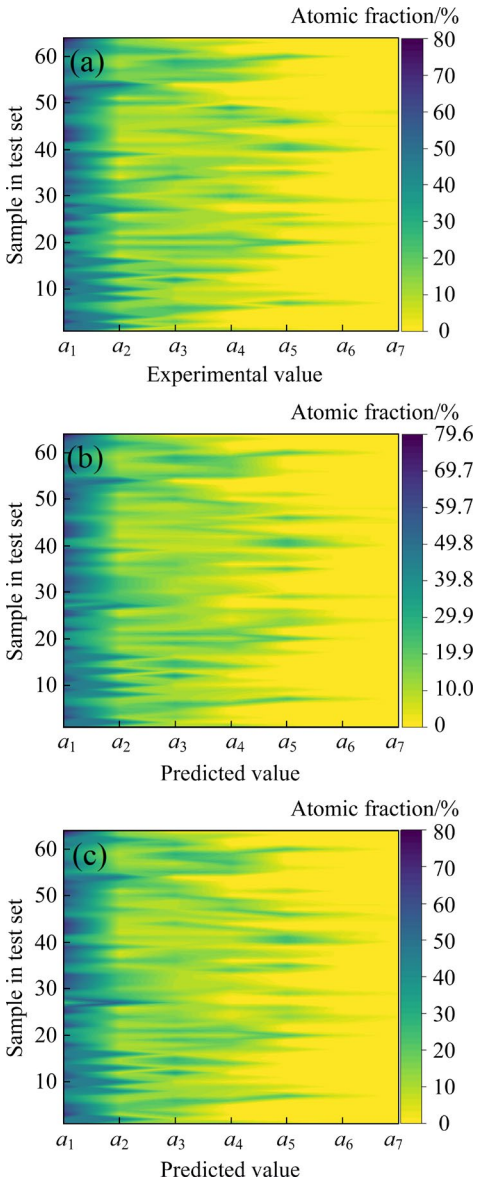

Fig. 10 Data for plotting two-dimensional cloud plot: (a) Experimental value; (b) Predicted value through DKIDNs model; (c) Predicted value through RIDNs model

cloud plot drawn from the experimental-value data. In order to quantify the similarity between the images, we calculate the Wasserstein distance between Figs. 10(a) and 10(b), as well as between Figs. 10(a) and 10(c), with the results being 0.422 and 0.572, respectively. The smaller Wasserstein distance indicates that the two images are more similar. Thus, it is shown that the predicted values of the DKIDNs model are closer to the experimental values as compared to the RIDNs model. In addition, we plot a heat map of the absolute errors of the predicted and experimental values, as shown in Fig. 11. It can be seen from Fig. 11 that both the DKIDNs and RIDNs models show excellent predictive ability, and most of their absolute errors are concentrated between 0 and 5. However, the prediction accuracy of the DKIDNs model is significantly better than that of the RIDNs model for some of the samples (see the red circle mark in Fig. 11). Table 5 summarizes the two evaluation indexes of the DKIDNs and RIDNs models of training set and the unseen test sets. The results suggest that both the DKIDNs and RIDNs show good training ability in the training set, but the DKIDNs model shows more excellent generalization ability in the test set.

Next, we evaluate the performance of the DKIDNs and RIDNs from a local perspective. From Figs. 12(a−h), it can be clearly observed that the majority of data points are closely clustered around the central black dashed line, and the generalization ability of the DKIDNs model is significantly superior to that of RIDNs model. For instance, in the samples of binary, ternary, quaternary, and quinary alloys (comprising a total of 50 samples), the R^2 values increase by 1.04%, 9.51%, 0.94%, and 2.55%, respectively. However, as shown in Figs. 12(i−l), the generalization ability of the DKIDNs model is slightly lower than that of the RIDNs model in the datasets of six-component and seven-component alloys (totaling 14 samples). Specifically, the R^2 values decrease by 1.57% and 0.41%, respectively.

In conclusion, the case test with elastic moduli as the target property shows that the two types of inverse design models constructed are able to predict the atomic fractions of the corresponding elements very well. This changes the working mode of the traditional trial-and-error method and forward prediction models, significantly improving their optimization efficiency. In addition, the DKIDNs model has better prediction accuracy and robustness.

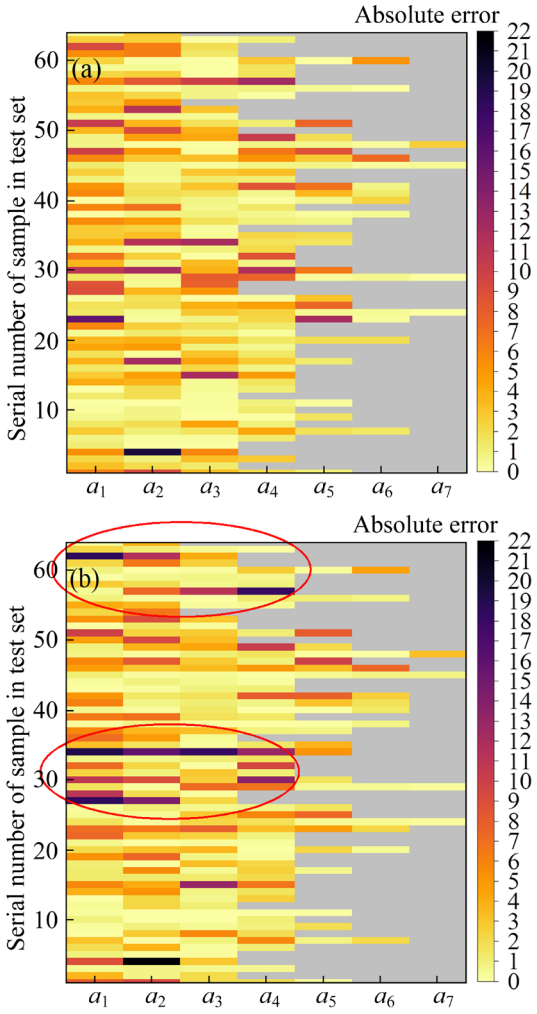

Fig. 11 Absolute error between experimental values and predicted values by DKIDNs (a) and RIDNs (b) models

Table 5 Consolidated results of DKIDNs and RIDNs models

Model	Training set		Test set	
	$\overline{\text{RMSE}}$	$\overline{R}^2$	$\overline{\text{RMSE}}$	$\overline{R}^2$
DKIDNs	4.624	0.926	9.071	0.907
RIDNs	4.624	0.918	10.341	0.860

3.3 Predictor−corrector inverse design scheme

After successfully constructing the forward prediction model and inverse prediction model, we use these two prediction models to design a predictor−corrector inverse design scheme (PCIDS), which provides theoretical guidance for the efficient development of novel amorphous alloys.

The PCIDS that can efficiently predict the atomic fractions of the corresponding elements

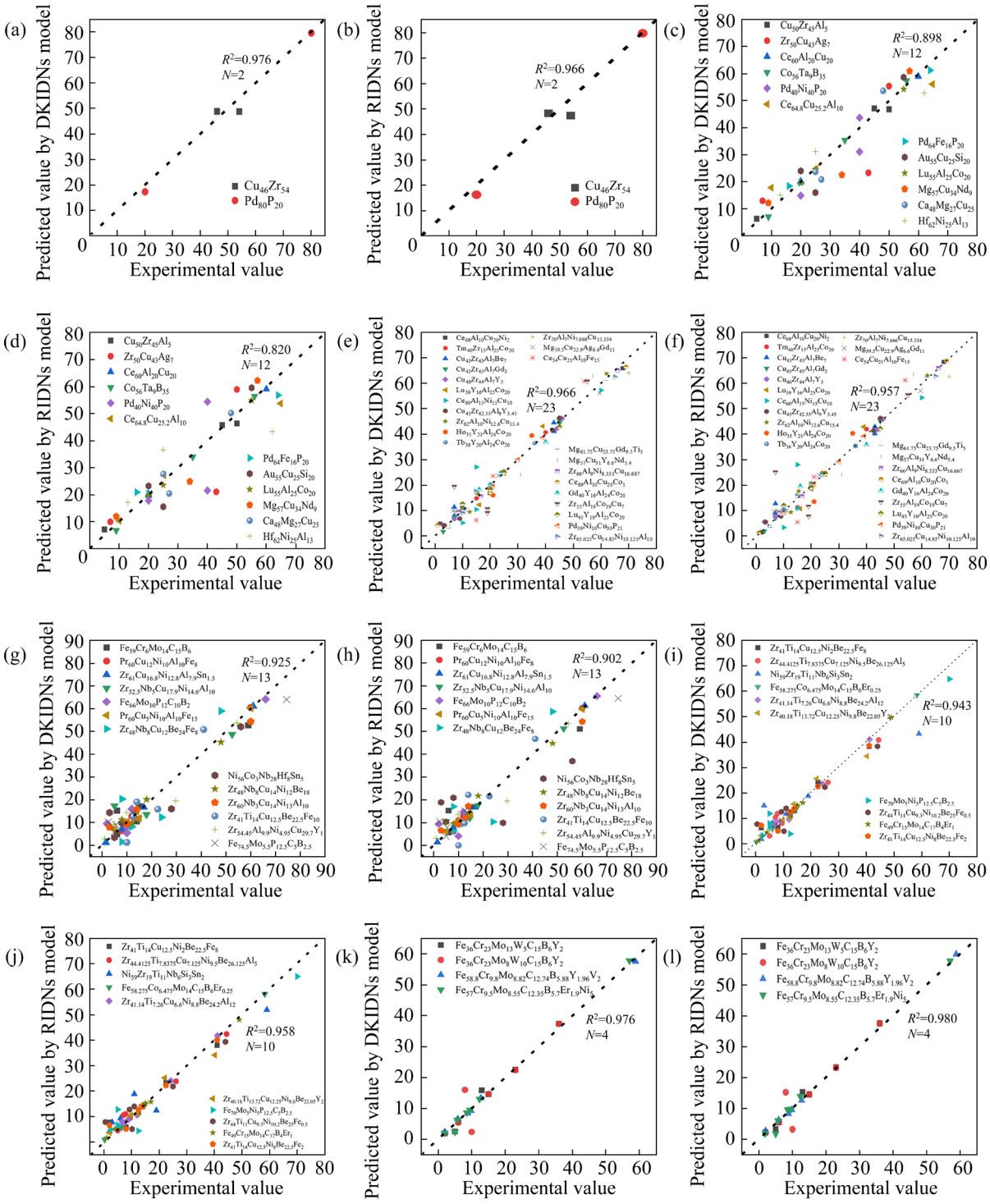

Fig. 12 Comparison of experimental and predicted values by DKIDNs and RIDNs models: (a, b) Binary alloys; (c, d) Ternary alloys; (e, f) Quaternary alloys; (g, h) Quinary alloys; (i, j) Six-component alloys; (k, l) Seven-component alloys (*N* represents the number of samples)

based on the user-specified element type and target property value is shown in Fig. 13. PCIDS consists of two parts, including the predictor module: (1) Input the specified element type and target properties values into the inverse prediction model; (2) Obtain the initial predicted value ***A*** by the inverse design model; (3) Input the initial predicted value ***A*** into the forward prediction model; (4) Determine whether the set target properties values are met based on the forward model

prediction results; (5) If satisfied, determine whether this alloy composition is capable of forming a BMGs via the GFA module; If not, using the corrector module; (6) Input the initial predicted value $\boldsymbol{A}$ to the corrector module; (7) Determine whether this alloy composition is capable of forming a BMGs via the GFA module; (8) If not, continue to use the corrector module; (9) If yes, output result. Note that the pseudo-code for the corrector module is shown in Algorithm 2. The GFA module is obtained by modifying our previous research work on the prediction of GFA for BMGs [20], details of which can be found in Note 1 of the Supplementary Information.

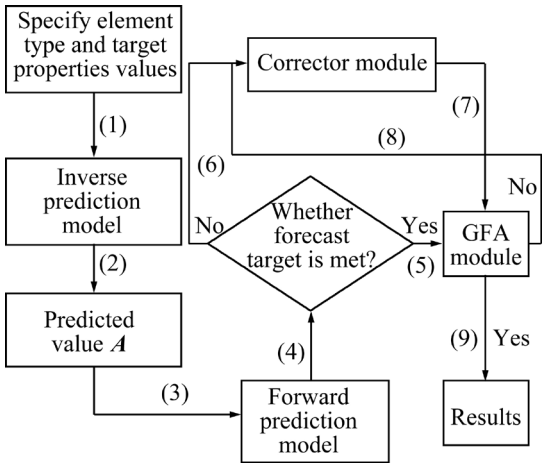

Fig. 13 Flow chart of PCIDS

Algorithm 2: Corrector Module

Input: Predicted value $\boldsymbol{A}=(a_1, a_2, \cdots, a_n)$ and the set target attribute value $\boldsymbol{Y}$;

Output: The optimal result after correction $\tilde{\boldsymbol{A}}=(\tilde{a}_1, \tilde{a}_2, \cdots, \tilde{a}_n)$;

1. Set calibration size E and step size h;

2. $\vec{a}_i \leftarrow a_i+E$ is the maximum value, a_i-E is the minimum value, and the step size is h, to obtain the compositions space;

3. $\vec{\boldsymbol{A}} \leftarrow$ Get the possible combinations of $(\vec{a}_1, \vec{a}_2, \cdots, \vec{a}_n)$;

4. $\vec{\boldsymbol{A}} \leftarrow$Retain all combinations that satisfy condition $\sum_{i=1}^{n} a_i = 100$ and $a_i > 0$;

5. $\tilde{\boldsymbol{Y}} \leftarrow$Input $\vec{\boldsymbol{A}}$ to the forward prediction model to obtain the target property prediction value $\tilde{\boldsymbol{Y}}$;

6. $\tilde{\boldsymbol{A}} \leftarrow$ Get the combination of compositions corresponding to $|\boldsymbol{Y}-\tilde{\boldsymbol{Y}}|_{\min}$;

7. Return result.

To further demonstrate the program process and illustrate its effectiveness, a case study is used to demo and validate. Suppose an alloy is specified to contain four elements, Ti, Zr, Be and Fe, and the target properties G=36 GPa and K=105 GPa need to be achieved. Notably, the Ti−Zr−Be−Fe alloy system does not appear in the original training set. To begin with, the predictor module results in a predicted composition of $Ti_{44}Zr_{22}Be_{30}Fe_4$, with predicted values of 38.18 GPa and 105.62 GPa for G and K, respectively. It can be calculated that the errors of the predicted values of G and K with respect to the set target values are 2.18 and 0.62, respectively. The error of the displayed G differs from our expected value. For this purpose, we use the corrector module to calibrate the alloy $Ti_{44}Zr_{22}Be_{30}Fe_4$.

According to Algorithm 2, we set the correction size E=5 and the step size h=1. Thus, we can obtain the ranges [39, 40, ⋯, 49] for Ti, [17, 18, ⋯, 27] for Zr, [25, 26, ⋯, 35] for Be and [−1, 1, ⋯, 9] for Fe. Next, we keep the combinations that satisfy the conditions among possible combinations used according to Steps 3 and 4 of the Algorithm 2 to obtain $\boldsymbol{A}$ containing 750 combinations. Figure 14 shows the parallel coordinates of the atomic fractions of Ti, Zr, Be and Fe. The redder the color, the larger the error between the predicted and set values of G for that composition combination, and vice versa, the bluer the color, the smaller the error. Finally, the best combination of $Ti_{42}Zr_{27}Be_{27}Fe_4$ is obtained. We input $Ti_{42}Zr_{27}Be_{27}Fe_4$ alloy into the forward prediction model, and the predicted values of G and K are 36.0006 GPa and 105.266 GPa, respectively, with errors of 0.0006 and 0.266 from the set target values. Finally, alloy $Ti_{42}Zr_{27}Be_{27}Fe_4$ is known to be

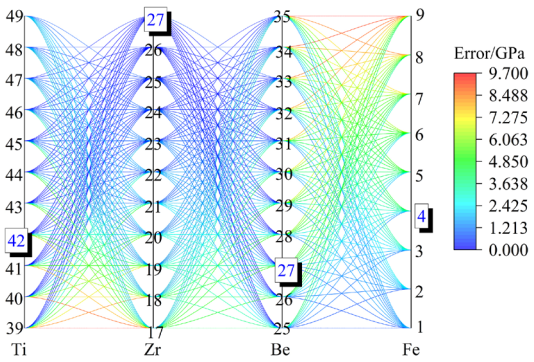

Fig. 14 Parallel coordinates of atomic fraction of Ti, Zr, Be and Fe

predicted by the GFA module to have a D_{max} greater than 2 mm.

To verify the accuracy of the conclusions, we collected relevant experimental data from the literature [52] for the Ti−Zr−Be−Fe alloy system and found that the reported G for alloy $Ti_{41}Zr_{25}Be_{28}Fe_6$ was 36.525 GPa. Since its K value was not reported directly, we calculated K as approximately 108.77 GPa by using Eq. (2) through the reported Poisson's ratio of ν=0.349 and G=36.525 GPa. Figure 15 shows a comparison of the $Ti_{41}Zr_{25}Be_{28}Fe_6$ alloy with the alloys predicted. A high correlation can be seen between the predicted alloy composition and the experimental composition. This confirms that the inverse design scheme based on our development plays an effective role in designing amorphous alloys with the specified properties.

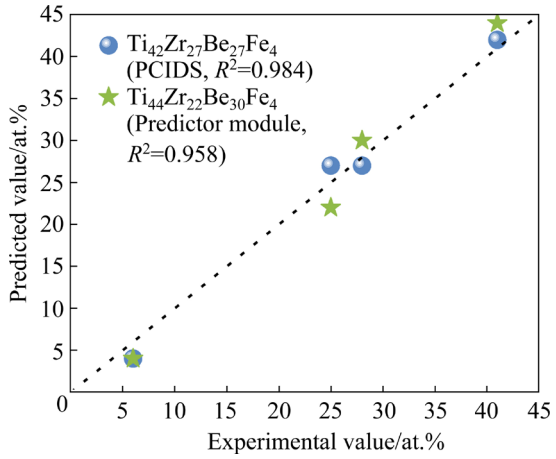

Fig. 15 Atomic fractions of two predicted alloy compositions compared with those of $Ti_{41}Zr_{25}Be_{28}Fe_6$ alloy reported in literature [52] (Note that $Ti_{44}Zr_{22}Be_{30}Fe_4$ alloy is only predicted by the predictor module and $Ti_{42}Zr_{27}Be_{27}Fe_4$ alloy is predicted by PCIDS)

4 Conclusions

(1) Highly accurate forward prediction models for bulk modulus K and shear modulus G based on DNNs have been developed.

(2) The SHAP analysis showed that the average atomic radius r exhibits a positive influence on both K and G when r is less than 147 pm. However, when the value of r exceeds 147 pm, it exerts a negative impact on K and G.

(3) The performance of the DKIDNs model, utilizing domain knowledge and fused with MSE as the loss function, surpasses that of the RIDNs model, which solely employs MSE as the loss function.

(4) PCIDS can expedite and effectively design amorphous alloy compositions with predetermined target properties. Moreover, PCIDS has broad applicability beyond amorphous alloys, offering innovative viewpoints for the advancement and design of other material fields.

CRediT authorship contribution statement

Tao LONG: Conceptualization, Visualization, Investigation, Formal analysis, Data curation, Writing – Original draft; **Zhi-lin LONG:** Conceptualization, Writing − Review & editing, Supervision; **Bo PANG:** Data curation.

Declaration of competing interest

The authors declare that they have no known competing financial interests or personal relationships that could have appeared to influence the work reported in this paper.

Acknowledgments

This research was supported by the National Natural Science Foundation of China (No. 52471184), the Science and Technology Major Project of Hunan Province, China (No. 2019GK1012), the Postgraduate Scientific Research Innovation Project of Xiangtan University, China (No. XDCX2023Y174), and the Postgraduate Scientific Research Innovation Project of Xiangtan University, China (No. XDCX2023Y173).

Supplementary Information

Supplementary Information in this paper can be found at: http://tnmsc.csu.edu.cn/download/12-p0169-2023-0575-Supplementary_Information.pdf.

References

[1] KLEMENT W, WILLENS R H, DUWEZ P O L. Non-crystalline structure in solidified gold−silicon alloys [J]. Nature, 1960, 187(4740): 869−870.

[2] JIAO Yu-zhang, DMITRY V L L, YAO Ke-fu, ZHANG Zheng-jun, CHEN Na. A room-temperature magnetic semiconductor from a Co−Fe−Nb−B metallic glass [J]. Science China Physics, Mechanics & Astronomy, 2023, 66(4): 246111.

[3] TELFORD M. The case for bulk metallic glass [J]. Materials Today, 2004, 7(3): 36−43.

[4] ZHAO Hang, ZHOU Jing, LIU Xiao, SHANG Bao-shuang, YAN Yu-qiang, DING Yong, SUN Bao-an, ZHANG Bo, KE Hai-bo, BAI Hai-yang, WANG Wei-hua. High-strength and malleable dual-phase nanostructured Ta-based metallic glass via atomic manufacturing [J]. Science China Materials, 2023, 66(11): 4226−4232.

[5] NG H W, HASEGAWA R, LEE A C, LOWDERMILK L A. Amorphous alloy core distribution transformers [J]. Proceedings of the IEEE, 1991, 79(11): 1608−1623.

[6] INOUE A, NISHIYAMA N. New bulk metallic glasses for applications as magnetic-sensing, chemical, and structural materials [J]. MRS Bulletin, 2007, 32(8): 651−658.

[7] ISMAGILOV F R, PAPINI L, VAVILOV V E, GUSAKOV D V. Design and performance of a high-speed permanent magnet generator with amorphous alloy magnetic core for aerospace applications [J]. IEEE Transactions on Industrial Electronics, 2019, 67(3): 1750−1758.

[8] WANG Wei-hua. Roles of minor additions in formation and properties of bulk metallic glasses [J]. Progress in Materials Science, 2007, 52(4): 540−596.

[9] DING Da-wei, TAN Jing, CAI An-hui, LIU Yong, WU Hong, AN Qi, LI Peng-wei, ZHANG Yan, YANG Qing. Fe-C micro-alloying effect on properties of $Zr_{53}Al_{11.6}Ni_{11.7}Cu_{23.7}$ bulk metallic glass [J]. Transactions of Nonferrous Metals Society of China, 2021, 31(9): 2750−2761.

[10] WANG Ming-zi, GUO Wei, LÜ Shu-lin, WU Shu-sen. Effect of deep cryogenic cycling treatment on structure and properties of metallic glass: A review [J]. Transactions of Nonferrous Metals Society of China, 2023, 33(10): 2879−2897.

[11] HART G L, MUELLER T, TOHER C, CURTAROLO S. Machine learning for alloys [J]. Nature Reviews Materials, 2021, 6(8): 730−755.

[12] YANG Chen, REN Chang, JIA Yue-fei, WANG Gang, LI Min-jie, LU Wen-cong. A machine learning-based alloy design system to facilitate the rational design of high entropy alloys with enhanced hardness [J]. Acta Materialia, 2022, 222: 117431.

[13] WU Yi-cheng, XU Bin, ZHANG Xue-feng, GUAN Peng-fei. Machine-learning inspired density-fluctuation model of local structural instability in metallic glasses [J]. Acta Materialia, 2023, 247: 118741.

[14] SAMAVATIAN M, GHOLAMIPOUR R, SAMAVATIAN V. Discovery of novel quaternary bulk metallic glasses using a developed correlation-based neural network approach [J]. Computational Materials Science, 2021, 186: 110025.

[15] SUN Y T, BAI H Y, LI M Z, WANG W H. Machine learning approach for prediction and understanding of glass-forming ability [J]. The Journal of Physical Chemistry Letters, 2017, 8(14): 3434−3439.

[16] LIU Xiao-wei, LONG Zhi-lin, YANG Ling-ming, ZHANG Wei, LI Zhuang. Prediction of glass forming ability in amorphous alloys based on different machine learning algorithms [J]. Journal of Non-crystalline Solids, 2021, 570: 121000.

[17] LIU X W, LONG Z L, ZHANG W, YANG L M. Key feature space for predicting the glass-forming ability of amorphous alloys revealed by gradient boosted decision trees model [J]. Journal of Alloys and Compounds, 2022, 901: 163606.

[18] XIONG Jie, ZHANG Tong-yi. Data-driven glass-forming ability criterion for bulk amorphous metals with data augmentation [J]. Journal of Materials Science & Technology, 2022, 121: 99−104.

[19] ZHANG Ting, LONG Zhi-lin, PENG Li, LI Zhuang. Prediction of glass forming ability of bulk metallic glasses based on convolutional neural network [J]. Journal of Non-Crystalline Solids, 2022, 595: 121846.

[20] LONG Tao, LONG Zhi-lin, PANG Bo, LI Zhuang, LIU Xiao-wei. Overcoming the challenge of the data imbalance for prediction of the glass forming ability in bulk metallic glasses [J]. Materials Today Communications, 2023, 35: 105610.

[21] CHEN Chun-teh, GU G X, Generative deep neural networks for inverse materials design using backpropagation and active learning [J]. Advanced Science, 2020, 7(5): 1902607.

[22] FRANCESCHETTI A, ZUNGER A. The inverse band-structure problem of finding an atomic configuration with given electronic properties [J]. Nature, 1999, 402(6757): 60−63.

[23] POLLOK S, BJORK R, JORGENSEN P S. Inverse design of magnetic fields using deep learning [J]. IEEE Transactions on Magnetics, 2021, 57(7): 1−4.

[24] JIANG Wei-feng, ZHU Yang-yang, YIN Guo-fu, LU Hou-hong, XIE Luo-feng, YIN Ming. Dispersion relation prediction and structure inverse design of elastic metamaterials via deep learning [J]. Materials Today Physics, 2022, 22: 100616.

[25] WNAG Chang-sheng, FU Hua-dong, JIANG Lei, XUE De-zhen, XIE Jian-xin. A property-oriented design strategy for high performance copper alloys via machine learning [J]. NPJ Computational Materials, 2019, 5(1): 87.

[26] ZHOU Zi-qing, SHANG Ying-hui, LIU Xiao-di, YANG Yong. A generative deep learning framework for inverse design of compositionally complex bulk metallic glasses [J]. NPJ Computational Materials, 2023, 9(1): 15.

[27] HE Tian-hao, ZHANG Dong-xiao. Deep learning of dynamic subsurface flow via theory-guided generative adversarial network [J]. Journal of Hydrology, 2021, 601: 126626.

[28] LU Shuai-hua, ZHOU Qiong-hua, CHEN Xin-yu, SONG Zhi-long, WANG Jin-lan. Inverse design with deep generative models: Next step in materials discovery [J]. National Science Review, 2022, 9(8): 15−17.

[29] DENG Chang-yu, JI Xun-bi, RAINEY C, ZHANG Jian-yu, LU Wei. Integrating machine learning with human knowledge [J]. Iscience, 2020, 23(11): 101656.

[30] MURDOCK R J, KAUWE S K, WANG A Y T, SPARKS T D. Is domain knowledge necessary for machine learning materials properties? [J]. Integrating Materials and Manufacturing Innovation, 2020, 9: 221−227.

[31] WEI Qing-hua, CAO Bin, DENG Lu-cheng, SUN An-kang, DONG Zi-qiang, ZHANG Tong-yi. Discovering a formula for the high temperature oxidation behavior of FeCrAlCoNi based high entropy alloys by domain knowledge-guided machine learning [J]. Journal of Materials Science & Technology, 2023, 149: 237−246.

[32] LI Xin, SHAN Guang-cun, ZHAO Hong-bin, SHEK Chan-hung. Domain knowledge aided machine learning method for properties prediction of soft magnetic metallic glasses [J]. Transactions of Nonferrous Metals Society of China, 2023, 33(1): 209−219.

[33] YANG Ming, LIU Xiong-jun, WU Yuan, WANG Hui, WANG Jian-biao, RUAN Hai-hui, LU Zhao-ping. Elastic modulus change and its relation with glass-forming ability and plasticity in bulk metallic glasses [J]. Scripta Materialia,

2019, 161: 62−65.
[34] WANG Wei-hua. The elastic properties, elastic models and elastic perspectives of metallic glasses [J]. Progress in Materials Science, 2012, 57(3): 487−656.
[35] WANG Wei-hua. Correlations between elastic moduli and properties in bulk metallic glasses [J]. Journal of Applied Physics, 2006, 99(9): 093506.
[36] CHEN Xing-qiu, NIU Hai-yang, LI Dian-zhong, LI Yi-yi. Modeling hardness of polycrystalline materials and bulk metallic glasses [J]. Intermetallics, 2011, 19(9): 1275−1281.
[37] XIONG Jie, SHI San-qiang, ZHANG Tong-yi. A machine-learning approach to predicting and understanding the properties of amorphous metallic alloys [J]. Materials & Design, 2020, 187: 108378.
[38] LI Zhuang, LONG Zhi-lin, LEI Shan, TANG Yu-lin. Machine learning driven rationally design of amorphous alloy with improved elastic models [J]. Materials & Design, 2022, 220: 110881.
[39] DUAN Gang, LIND M L, BLAUWE K D, WIEST A, JOHNSON W L. Thermal and elastic properties of Cu−Zr−Be bulk metallic glass forming alloys [J]. Applied Physics Letters, 2007, 90(21): 211901.
[40] FANG Shou-shi, XIAO Xue-shan, XIA Lei, LI Wei-huo, DONG Yuan-da. Relationship between the widths of supercooled liquid regions and bond parameters of Mg-based bulk metallic glasses [J]. Journal of Non-Crystalline Solids, 2003, 321(1/2): 120−125.
[41] SRIVASTAVA N, HINTON G, KRIZHEVSKY A, SUTSKEVER I, SALAKHUTDINOV R. Dropout: A simple way to prevent neural networks from overfitting [J]. The Journal of Machine Learning Research, 2014, 15(1): 1929−1958.
[42] MADUABUCHI C, ENEH C, ALROBAIAN A A, ALKHEDHER M. Deep neural networks for quick and precise geometry optimization of segmented thermoelectric generators [J]. Energy, 2023, 263: 125889.
[43] RAISSI M, PERDIKARIS P, KARNIADAKIS G E. A deep learning framework for solving forward and inverse problems involving nonlinear partial differential equations [J]. Journal of Computational physics, 2019, 378: 686−707.
[44] KARNIADAKIS G E, KEVREKIDIS I G, LU L, PERDIKARIS P, WANG S, YANG L. Physics-informed machine learning [J]. Nature Reviews Physics, 2021, 3(6): 422−440.
[45] DUCHI J, HAZAN E, SINGER Y. Adaptive subgradient methods for online learning and stochastic optimization [J]. Journal of Machine Learning Research, 2011, 12(7): 257−269.
[46] XIONG Jie, ZHANG Tong-yi, SHI San-qiang. Machine learning prediction of elastic properties and glass-forming ability of bulk metallic glasses [J]. MRS Communications, 2019, 9(2): 576−585.
[47] LUNDBERG S M, LEE S I. A unified approach to interpreting model predictions [J]. Advances in Neural Information Processing Systems, 2017, 30: 4768−4777.
[48] ZHAN W, CHENG J L, FENG S D, LI G, LIU R P. Intrinsic correlation between elastic modulus and atomic bond stiffness in metallic glasses [J]. Materials Letters, 2016, 175: 227−230.
[49] ZHAO W, LI G, WANG Y Y, FENG S D, QI L, MA M Z, LIU R P. Atomic bond proportions and relations to physical properties in metallic glasses [J]. Materials & Design, 2015, 65: 1048−1052.
[50] PANG J J, TAN M J, LIEW K M. On valence electron density, energy dissipation and plasticity of bulk metallic glasses [J]. Journal of Alloys and Compounds, 2013, 577: S56−S65.
[51] YANG Wei-ming, SUN Xin-fa, LIU Hai-shun, YU Chang-feng, LI Wen-yu, INOUE A, ŞOPU D, ECKERT J, TANG Chun-guang. Structural homology of the strength for metallic glasses [J]. Journal of Materials Science & Technology, 2021, 81: 123−130.
[52] GU Jia-lun, SHAO Yang, YAO Ke-fu, The novel Ti-based metallic glass with excellent glass forming ability and an elastic constant dependent glass forming criterion [J]. Materialia, 2019, 8: 100433.

预估−校正逆向设计方案用于非晶合金性能−成分预测

龙 滔[1]，龙志林[2]，庞 博[1]

1. 湘潭大学 机械工程与力学学院，湘潭 411105；
2. 湘潭大学 土木工程学院，湘潭 411105

摘 要：为了开发一种通用框架，使其能够设计出具有所需目标性能的新型非晶合金，提出了一种由预测模块和校正模块组成的预估−校正逆向设计方案(PCIDS)。为实现这两个部分，开发了基于深度神经网络的高精度正向预测模型。最重要的是，还开发了领域知识引导的逆向设计网络(DKIDNs)和常规逆向设计网络(RIDNs)。在测试集上，正向预测模型关于剪切模量和体积模量的决定系数(R^2)分别为 0.990 和 0.986。此外，与 RIDNs 模型相比，DKIDNs 模型表现出更优越的预测性能。最终，证明 PCIDS 可以高效预测出所需目标性能的非晶合金成分。

关键词：非晶合金；机器学习；深度神经网络；逆向设计；弹性模量

(Edited by Bing YANG)